Contents lists available at ScienceDirect

Nuclear Inst. and Methods in Physics Research, A

journal homepage: www.elsevier.com/locate/nima

Performance of the DAMPE BGO calorimeter on the ion beam test

Yifeng Wei, Yunlong Zhang *, Zhiyong Zhang, Libo Wu, Sicheng Wen, Haoting Dai, Chenming Liu, Xiaolian Wang, Zizong Xu, Guangshun Huang *, Changqing Feng, Shubin Liu, Qi An

State Key Laboratory of Particle Detection and Electronics, University of Science and Technology of China, Hefei 230026, China
Department of Modern Physics, University of Science and Technology of China, Hefei 230026, China

ARTICLE INFO

ABSTRACT

The DArk Matter Particle Explorer (DAMPE), which is a Chinese space telescope for the precise measurement of high-energy electrons, gamma rays, and nuclei from deep space, was successfully launched on December 17, 2015. The DAMPE electromagnetic calorimeter made of bismuth germanium oxide (BGO) crystals can measure incident hadron energies from 50 GeV to 100 TeV. The calorimeter was tested with ion beams at CERN in 2015. The energy responses to ions from helium to argon are investigated. The result is reproduced by a Monte Carlo simulation based on Geant4 with two physics process models. It shows that the simulation results of a beam test are independent of the physics models adopted. Additionally, quenching effects of the BGO crystal on the ions are observed with this beam test. The quenching attenuations increase with the atomic number and were approximately 7% for boron and 40% for argon.

1. Introduction

Several recent astro-particle physics experiments have reported some anomalous phenomena in cosmic-ray flux, for example, electron and positron excesses beyond 100 GeV [1–3], a tentative ~130 GeV gamma-ray line [4] and a remarkable hardening of cosmic-ray nuclei spectra at the magnetic rigidity of several hundreds of GV [5–9]. These additional structures may be caused by some unknown sources of cosmic ray, or dark matter decay/annihilation.

The DArk Matter Particle Explorer (DAMPE) [10] is a high-energy cosmic-ray and gamma-ray telescope. It was launched into a sun-synchronous orbit at an altitude of 500 km on December 17, 2015. DAMPE is able to extend the energy range of space-based particle detectors to tens of TeV region with a high energy resolution. The main objectives of DAMPE are as follows: (1) to search for a signature of dark matter particles, (2) to understand the origin, propagation, and acceleration mechanisms of high-energy cosmic rays, and (3) to study the gamma-ray emission from galactic and extragalactic sources.

The DAMPE detector is composed of a Plastic Scintillator Strip Detector (PSD), a Silicon–Tungsten Tracker (STK), a Bismuth Germanium Oxide (BGO) calorimeter and a NeUtron Detector (NUD), as shown in Fig. 1. The charge, trajectory, and the energy of incident particles are measured using the PSD, the STK, and the BGO calorimeter, respectively. The calorimeter also identifies cosmic ray electrons from massive hadron background, and the NUD improves the electron/hadron separation.

To investigate the detector performance, a full-size DAMPE detector model, called the Engineering Qualification Model (EQM), was extensively tested with different particle beams at CERN in 2014 and 2015. This paper presents the energy response of the calorimeter to various species of ions, as well as the ionizing energy loss in the calorimeter layer. Monte Carlo (MC) simulations are conducted to be compared with the experimental data.

2. Design of the BGO calorimeter

The BGO calorimeter is the core sub-detector of DAMPE and measures the energy of incident particles with high energy resolution. The calorimeter consists of 14 layers, and each layer contains 22 BGO crystal bars with an individual size of $25 \times 25 \times 600$ mm³ (Fig. 2). The adjacent layers are arranged perpendicularly to reconstruct the shower topology in the calorimeter. Each end of a crystal is coupled to a Hamamatsu R5610A-01 photo-multiplier tube (PMT) (see Fig. 3). To achieve a large dynamic range, three dynodes (dynodes 2, 5, and 8) of the PMT are read out, which correspond to low, middle, and high gain, respectively. A 32-channel Application Specific Integrated Circuits (ASIC), named VA160 (or VATA160 for the bars that generate the trigger) [11] are chosen as the chip of Front-End Electronics (FEE); it is composed of a charge-sensitive pre-amplifier, a CR-RC shaping amplifier, and a sample-hold circuit. The FEEs receive the current signals of the PMT dynodes, integrate the charges and digitize them with a 16-bit ADC
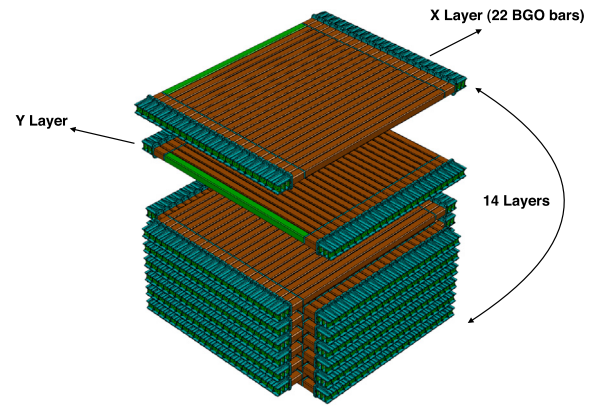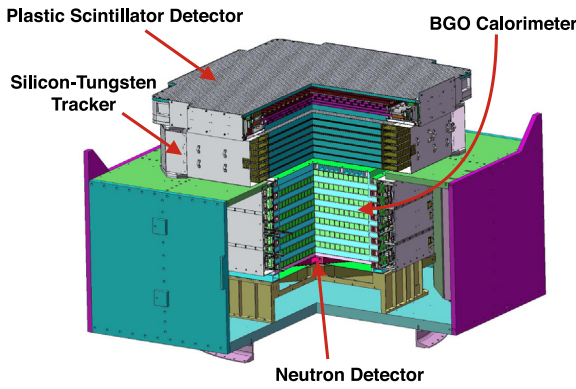
Fig. 2. The BGO-crystal bar arrangement in the calorimeter. There are 14 layers, each layer containing 22 BGO crystal bars.

Fig. 3. Schematic graph of the BGO calorimeter readout. Both ends of each BGO bar are coupled with a PMT that has three different dynode readouts.
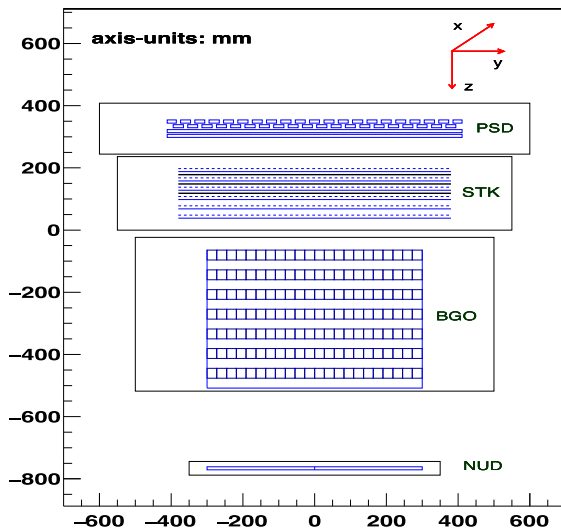
Fig. 1. Schematic view of DAMPE (top). It is composed of a Plastic Scintillator Detector (PSD), a Silicon–Tungsten Track (STK), a BGO calorimeter (BGO), and a NeUtron Detector (NUD). The structure diagram of the DAMPE detector (bottom).
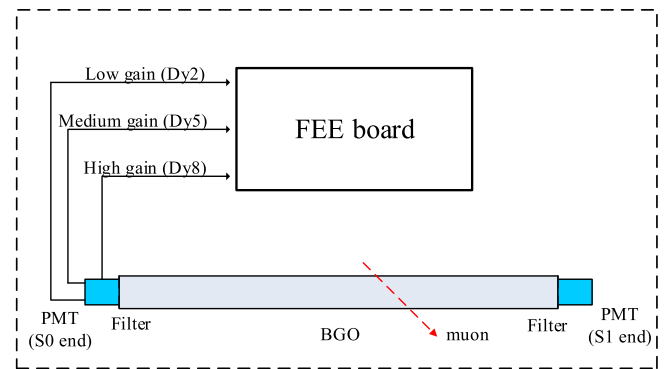
(AD976A) [12]. In an FEE board, a calibration circuit is also designed to monitor the performance of the VA160 chip. Detailed information on the readout system and electronics can be found in Ref. [13–16].

3. Beam test at CERN-SPS

In March 2015, the EQM of DAMPE was tested with various species of ions on H8 beamline at the CERN Super Proton Synchrotron (SPS) facility. The primary particles, 40Ar, were provided with momenta of 40 and 75 GeV/nucleon (GeV/n), and they impacted on a 40-mm-thick polyethylene target to produce secondary ions. The secondary

fragments were transported up to the rigidity selection magnet. The selected events had the same velocity as the primary particles and had the characteristics of A/Z=2. Fig. 4 shows the beam test configuration. A series of ancillary detectors were positioned upstream of the DAMPE detector on the beamline. S1 and S2 were finger scintillators that provided the external trigger for the whole detector system. To reduce the data size, we raised the trigger threshold to suppress the trigger efficiency of proton and helium fragments. Si1 and Si2 were silicon pin detectors. These ancillary detectors made it possible to measure the dE/dx values of incident particles and distinguish the charges. The PSD and STK detectors also precisely measured of the charges; the details are presented in Ref. [10].

When an ion penetrated the detectors, it produced signals in the finger scintillators, silicon pin detectors, and PSD. After the pedestals were subtracted, the Analog-to-Digital Converter (ADC) counts of the
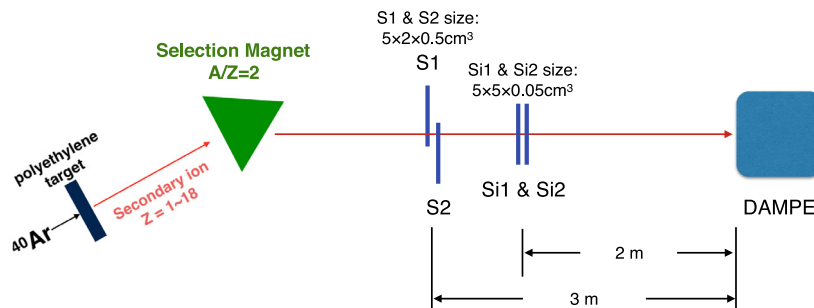

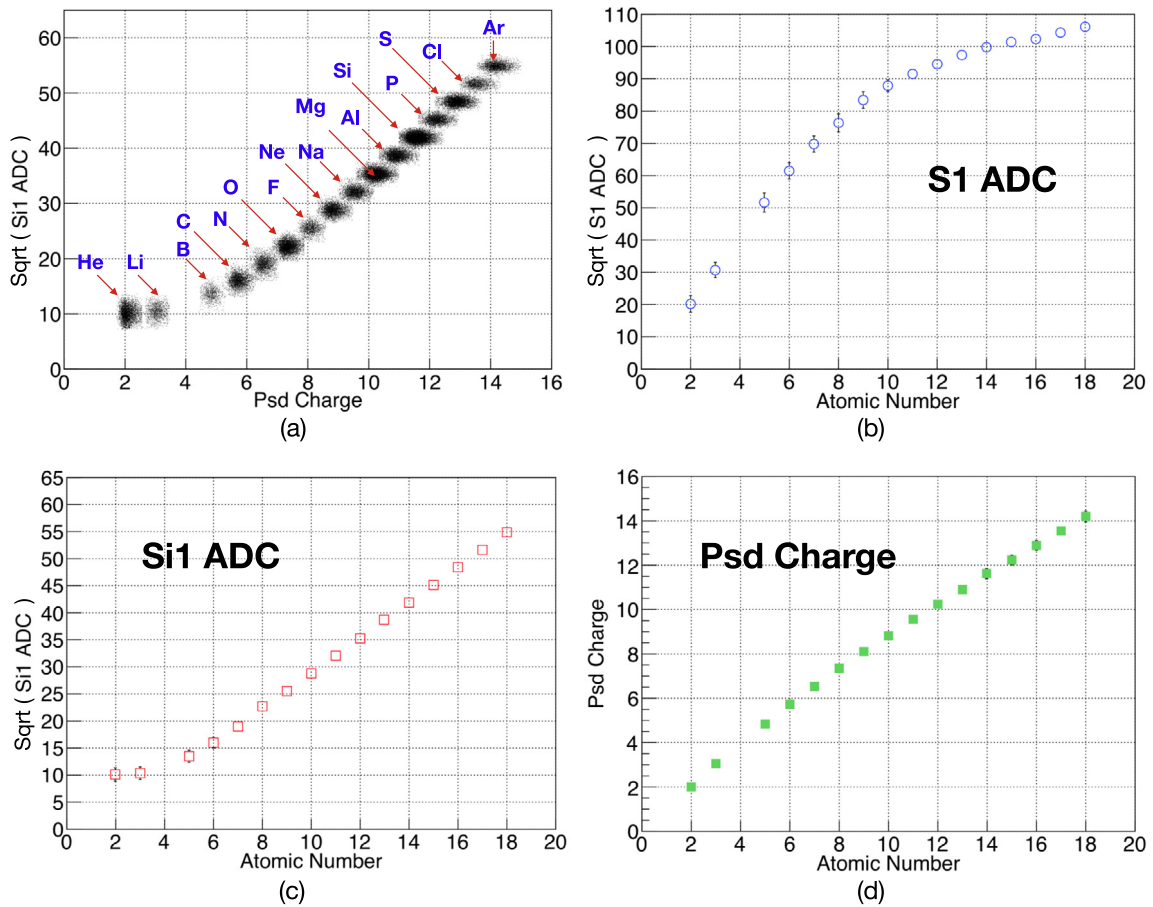**Fig. 4.** Configuration of the beam test instrument.

Fig. 5. (a) The correlation between the PSD charge and the square root of the Si1 ADC counts. The ions' mean values of the S1 (b), Si1 (c) and PSD (d) as functions of the atomic number.
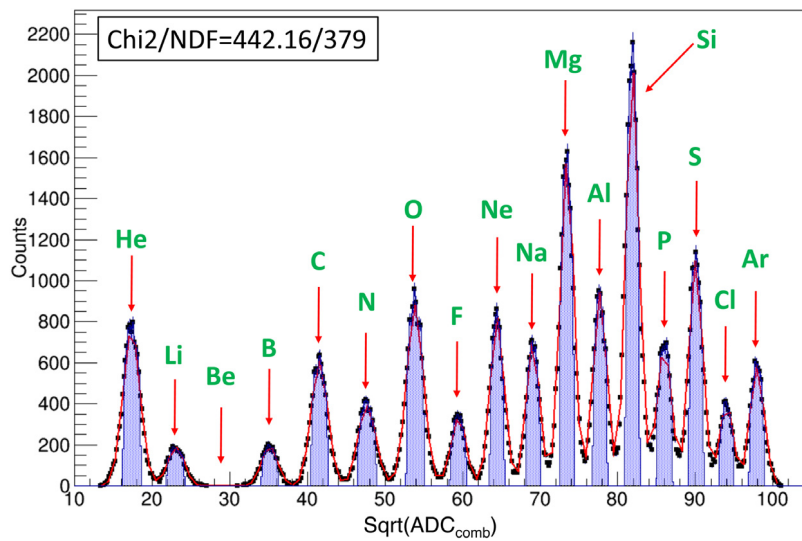

Fig. 6. $\sqrt{(ADC_{comb})}$ distribution for different ions. The black dots are experiment data, and the red line is fitted function. The blue area shows the one standard-deviation region around each ion peak.

finger scintillators and silicon pin detectors can be used as charge signature directly. For the PSD, the charge number can be determined by energy:

$$Z_{PSD} = \sqrt{\frac{E_{PSD}}{E_0}}$$

(1)

where E_{PSD} is the energy reconstructed by the PSD, E_0 is a normalization factor, corresponding to one proton minimum ionizing particle (MIP) energy of the PSD (2 MeV). This PSD charge number helps identify the relationship between the ion atomic number and the ADC counts for the other four ancillary detectors. Fig. 5(a) shows the correlation between the PSD charge and the square root of the Si1 ADC counts. Ion islands of all species can be easily distinguished. For a given ion
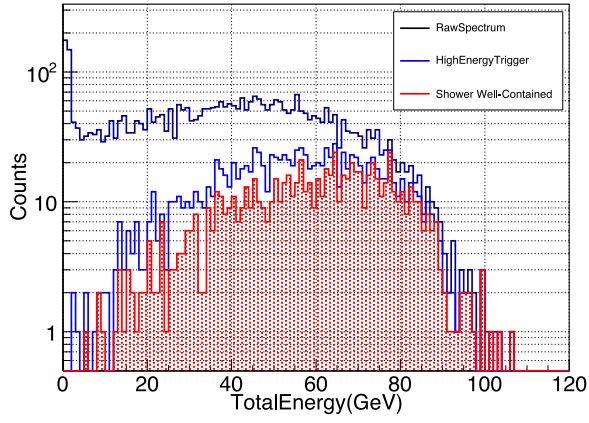
Fig. 7. Total energy in the calorimeter for 40 GeV/n helium.

$$+ K \times Z_{PSD}) \qquad (2)$$

$$K = \frac{\sqrt{ADC_{S1}} + \sqrt{ADC_{S2}}}{2 \times Z_{PSD}}\Bigg|_{Helium} = 10.33(\sqrt{channel}) \qquad (3)$$

where ADC_{S1}, ADC_{S2}, ADC_{Si1} and ADC_{Si2} presented the ADC counts of two finger scintillators and two silicon pin detectors, respectively, and Z_{PSD} is the charge reconstructed from the PSD. As shown in Fig. 5, the numerical value of the PSD charge is much smaller than that of the ADCs of the finger scintillators and the silicon pins. To balance their contributions, a weighting factor K is introduced here. It is defined as the ratio of the average helium peak ADC values of two finger scintillators over the PSD charge of helium.

Fig. 6 shows the $\sqrt{(ADC_{comb})}$ distribution for different ions (Z > 1). All of the elements from helium (Z = 2) to argon (Z = 18) can be clearly identified, except for the unstable isotope $^{8}_{4}Be$ (Z = 4). The spectrum is fitted by a sum of Gaussian distributions with different mean values, and events within one standard deviation around each peak (the blue area in Fig. 6) are selected as clean candidates of the element. The contaminations of particle identification are determined with the fitted function; they are always less than 1% for all kinds of ions.

The energy calibration of each signal from a BGO crystal is carried out by using the beam test results. Before the beam test, a long-duration cosmic-ray muon test was conducted, and a muon MIPs peak was utilized to calibrate the energy scale of each detector unit (BGO crystal + PMT). The pedestals were monitored once an hour with random triggers throughout the whole beam test duration. The gains of the PMT readout dynodes were calibrated with shower events of beam particles. Then, the deposited energies in the BGO bars were reconstructed based on the aforementioned calibration constants. Full details of the calorimeter calibration and reconstruction procedure on the ground are provided in Ref. [17].
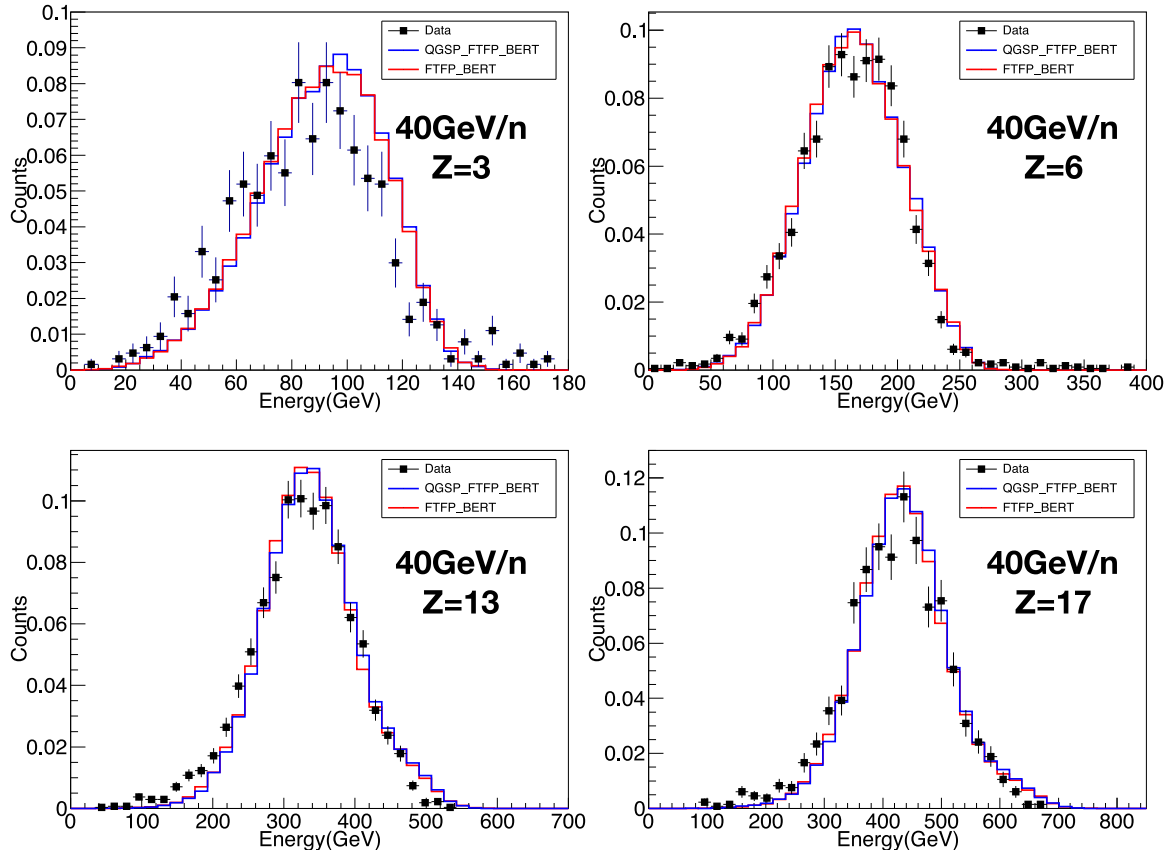
species, its corresponding PSD charge and Si1 ADC can be derived immediately from this figure. In this way, we have established a relationship between the Si1 ADC count and the atomic number. Analogously, this method also works for the other three detectors. In Fig. 5(b)–(d), such relationships for the S1 ADC, Si1 ADC, and PSD charge are presented respectively. A nonlinear response to heavy ions is observed for the finger scintillators, while for the silicon pin detectors, such nonlinearity occurs in the light ion region. The PSD charge also appears to be slightly nonlinear, due to the quenching effect of ions heavier than boron.

To take advantage of the signals of all these three kinds of charge detectors, a new variable "combined ADC" is defined as follows:

$$\sqrt{ADC_{comb}} = \frac{1}{3} \times (\frac{\sqrt{ADC_{S1}} + \sqrt{ADC_{S2}}}{2} + \frac{\sqrt{ADC_{Si1}} + \sqrt{ADC_{Si2}}}{2}$$

Fig. 8. Energy response to Z = 3, 6, 13 and 17 (40 GeV/n) ions for data (square points) compared to simulation using QGSP_FTFP_BERT (blue line) and FTFP_BERT (red line) physics lists.

Fig. 9. Energy response to Z = 3, 6, 13 and 17 (75 GeV/n) ions for data (square points) compared to simulation using QGSP_ FTFP_ BERT (blue line) and FTFP_ BERT (red line) physics lists.
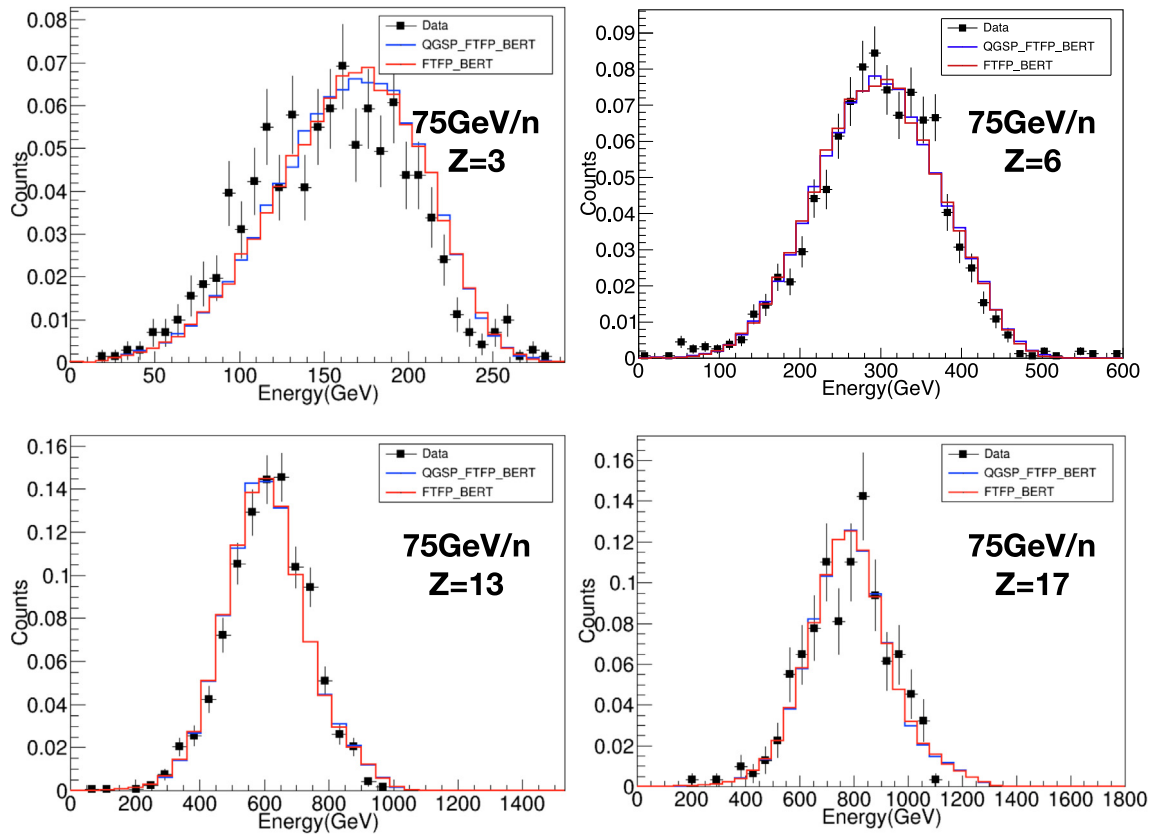
4. Energy response to shower events

The calorimeter response to ions is complicated. Basically, the energies of the hadronic shower, which can be detected by the calorimeter, are composed of two parts: one is the electromagnetic component, mainly from the production of π_0s and ηs and their subsequent decay to two photons; and the other is the hadronic component. Contributions from soft neutrons, neutrinos, and binding energy, etc., called "invisible energy", cannot create signals in the calorimeter. The invisible energy and the production of π_0s and ηs fluctuate from event to event, and affect the calorimeter signal, and hence the energy resolution. In this section, the BGO calorimeter response to ions is investigated with a beam test and validated with an MC simulation.

The DAMPE MC simulation software [18] was developed based on the Geant4 toolkit. To build a detailed detector model as true as possible to the physical detector, the geometry and materials information of all the detector units were constructed with Geometry Description Markup Language (GDML) and then imported into Geant4. Digitization algorithms were developed to convert the simulation energy hits into ADC counts, which also took into consideration the pedestal noise, PMT gains, and electronic fluctuation. These methods ensured the accuracy of the instrument response's description. The simulation data are saved in the same format as the real data so that the reconstruction algorithms apply to both the MC and experimental data.

4.1. Selection method

In this analysis, only events that fully develop in the calorimeter are selected. The selection criteria are as follows:

1. High energy trigger (HET) selection: HET, one of five group trigger logics of the DAMPE detector, requires that the energy

deposition in layer 1 of the calorimeter should be larger than the energy of 1 MIP (~22.5 MeV), and that the energy deposition in layer 2–4 should be higher than that of 10 MIPs. Events with showers starting in the first several layers are selected.

2. "Shower Well-Contained" selection: This selection requires that the shower maximum should be located before layer 10 of the calorimeter, to obtain the events in which longitudinal shower maximum is contained in the calorimeter.

In the normal incidence case, the tracking efficiency and lateral energy leakage of the calorimeter are not considered. The measured energy summed up for all of the crystals for 40 GeV/n helium is shown in Fig. 7. The black line is the raw energy deposit in the calorimeter; the blue line represents the energy spectrum after HET selection and the red area after both of the two criteria.

4.2. Energy spectra of ions

The energy spectra of several kinds of ions are shown in Figs. 8 and 9. The distributions are asymmetrical since the shapes of low energy tails depend on the selections applied on the raw energy spectra.

To compare with the real data and evaluate the calorimeter performance, simulations based on Geant4 were conducted with the same experimental conditions as the beam test. It is generally known that several "physics lists" are available in the Geant4 simulation toolkit; they combine different models in variable energy ranges. In this work, we performed two simulations based on the QGSP_ FTFP_ BERT and FTFP_ BERT physics lists, with the former applying the Quark Gluon String (QGS) model and the latter the Fritiof (FTF) model above 25 GeV. They are considered suitable in the beam test energy range. In Figs. 8 and 9, energy spectra simulated with physics lists QGSP_ FTFP_ BERT and FTFP_ BERT are illustrated as blue and red lines, respectively.
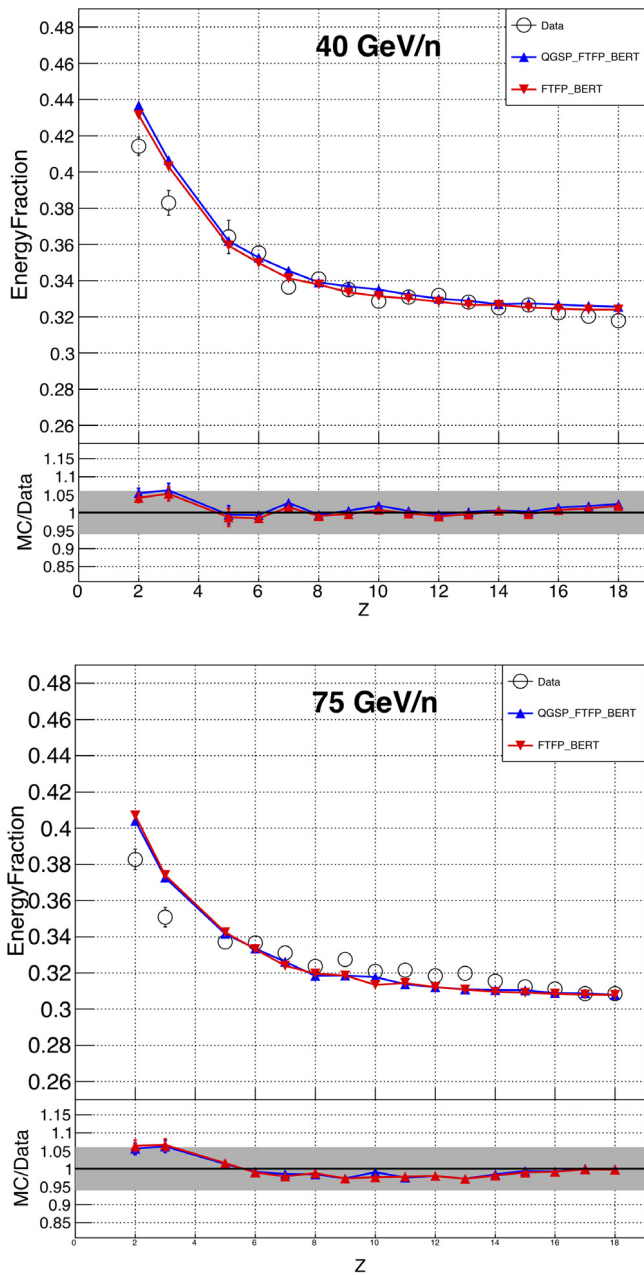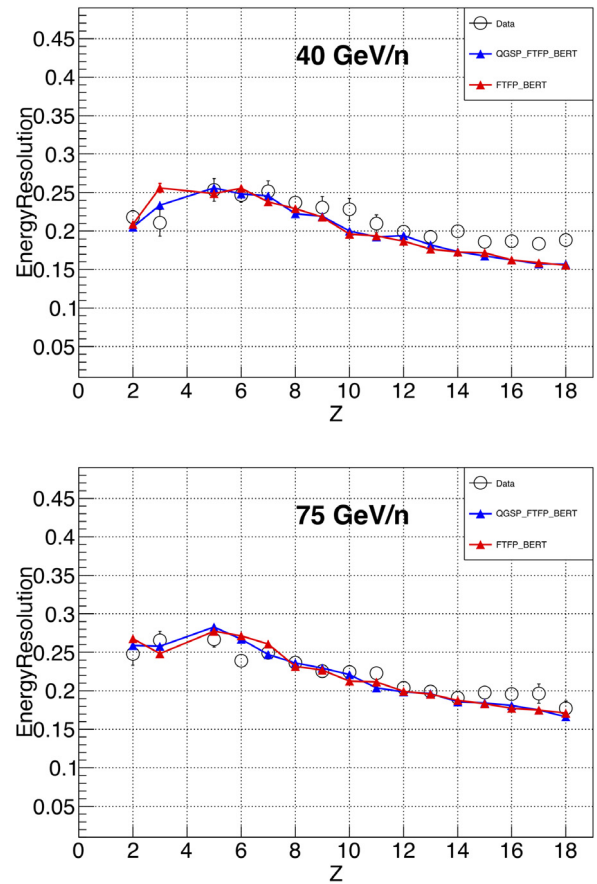
Fig. 11. Energy resolution as a function of the atomic number for a 40 GeV/n beam (top) and for a 75 GeV/n beam (bottom)

BERT are almost completely consistent, and the energy fractions have an agreement within a difference of < 1.3%.

For helium and lithium, at both energy points, the data and simulations with two physics lists are consistent within ~6% deviations. For higher atomic numbers, the agreement with the data improves, and the deviations are always < 3%. The maximum difference of those is 2.6% for 75 GeV/n aluminum. As shown in Fig. 11, the energy resolutions in the case of normal incidence are always better than 30% for all kinds of ions at these two energy points.

5. Ionizing energy loss in BGO crystal

Some ions only suffer ionization energy loss, yet do not induce nuclear reactions with calorimeter material. Quenching interactions of fluorescence photon number occur when ions pass through inorganic scintillators. At low ion incident energy, the quenching effect of BGO crystal was reported [19]. To the best of our knowledge, at the extremely high energy level, such an effect has not been reported in the literature. An unexpected anti-quenching effect of CsI(Tl) crystal in a Fermi Large Area Telescope beam test performed at the GSI Helmholtz Center for Heavy Ion Research was reported in Ref. [20]. The study reported that the quenching effect depended on both the species and the energy of the incident particle. In this section, we investigate the ionizing energy loss in a 25-mm-thick BGO calorimeter layer and discuss the quenching and anti-quenching effect with 40 and 75 GeV/n beams.

5.1. Selection method

The ionization events were used to study the quenching effect of ions. Given that the hadron interaction cross-section increases with the
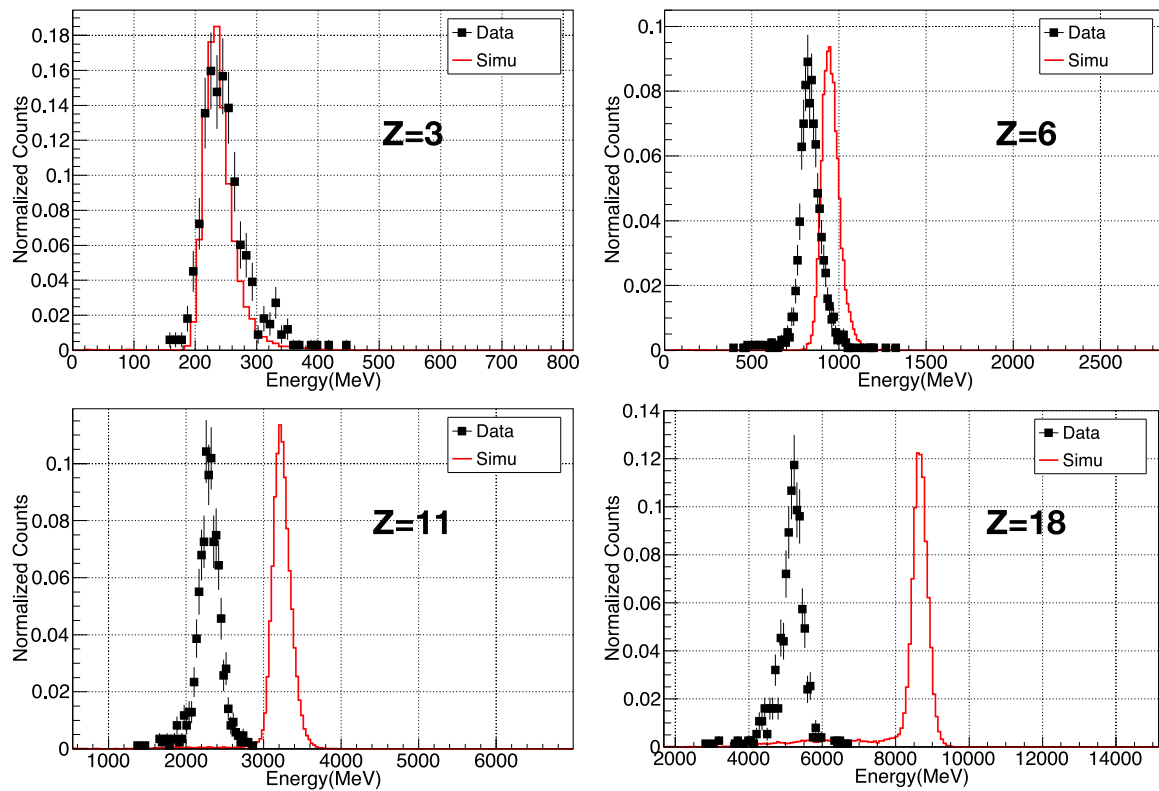

Fig. 10. Energy fraction as a function of the atomic number for a 40 GeV/n beam (top) and for a 75 GeV/n beam (bottom). The data and simulation results with two physics lists have a deviation of 6% at Z = 2 and 3 for both energy points. The differences are reduced for ions heavier than boron.

The MC simulation well simulates the shape of the response and the position of the peak for most kinds of ions. However, for some ions, such as helium and lithium, the energy spectra are slightly shifted from the MC simulation results.

Here we define the energy fraction as the peak energy of the deposition distribution divided by the beam energy of ions, to quantify the agreement between the data and the MC models. The energy fraction as a function of the atomic number is compared to the MC simulation in Fig. 10; it decreases with the atomic number from ~41.4% (helium) to ~31.8% (argon) for the 40 GeV/n beam. The energy fraction of the 75 GeV/n beam is lower than that of a 40 GeV/n beam for a given kind of ion, and is 38.5% for helium and 31.4% for argon. At these two energy points, the energy spectra of physics list QGSP_ FTFP_ BERT and FTFP_

Fig. 12. Comparison between the deposited energy distribution measured by the first layer of the calorimeter (black squares) and the energy spectrum predicted by Geant4 (red line) for the 40 GeV/n beam.

nucleon number A, it is impossible to select events for high-Z ions passing through the calorimeter from top to bottom. Therefore, we required that the incident particles should penetrate at least first N layers of the calorimeter as a single particle without creating a shower. N is chosen as two here to obtain sufficient statistics for the layer energy spectrum. The following conditions should be satisfied:

1. There should be no more than two bars fired in one layer; this layer is named as "penetrated layer".
2. The first two layers of the calorimeter should be penetrated layers.

Since Geant4 simulation has compelling descriptions for ionizing processes, only one physics list, QGSP_ FTFP_ BERT, was applied to study the quenching effect. The measured energy deposits in the first layer (black dots) compared to those provided by the MC simulation (red line) are displayed in Fig. 12 for Z = 3 (Li), Z = 6 (C), Z = 11 (Na) and Z = 18 (Ar). No path length correction needs to be applied as the particle traversed the crystal perpendicularly to the layer plane. For light ions, the energy deposition in a single calorimeter layer is well-described as a Landau distribution convoluted with a Gaussian distribution. The Landau tail results from a fraction of the lost energy that is carried off by energetic knock-on electrons (also known as δ electrons). For heavier ions, the distribution turns to a Gaussian because the effect of δ electrons is weakened with the growing number of individual collisions. Fig. 12 also indicates that, concerning energy, the MC and beam data are more in agreement for helium and lithium, while a significant separation occurs as the atomic number increases. This energy separation results from quenching.

5.2. Quenching effect of BGO

To quantitatively evaluate the quenching effect of BGO crystal, the quenching factor (ϵ) is defined as the ratio E_{Meas}/E_{MC}, where E_{Meas} is the measured energy for the ion and is proportional to the collected

light, and E_{MC} is the deposited energy in the MC simulation. The ionization energy spectra were fitted with a Gaussian convoluted Landau distribution for Z < 6 particles and with a Gaussian distribution for Z $\geq$ 6 ones. The same fitting procedure was also applied to the simulation data to yield the quenching factors of different ions. Fig. 13 shows the square root of the ionization peak energy as a function of the ion atomic number. The blue squares represent the beam data, and the open circles are the MC peak values, which could be well fitted with a linear function.

The measured quenching factors are shown as a function of the ion atomic number in Fig. 14. For helium and lithium, the quenching factors at 40 and 75 GeV/n are found to be nearly 1. For heavier ions starting from Z = 5, the measured energies are smaller than the calculated ones. Birk's attenuation ($1 - \epsilon$) increases from ~7% for boron to 40% for argon, indicating a strong dependence of the quenching factor on ion species. In this beam test, ($\epsilon > 1$) is not observed except for lithium with an energy of 40 GeV/n. However, the anti-quenching effect is not statistically significant because the quenching factor is 1.014 $\pm$ 0.013 (statistical error) for this case. In addition, there is little difference between the quenching factors at 40 and 75 GeV/n. This is far from sufficient to conclude whether or not the quenching factor is incident-energy-dependent, as the two sets of the data are too close regarding the magnitude of the incident energy.

6. Conclusion

The response of the DAMPE BGO calorimeter to ions is investigated at 40 and 75 GeV/n, using data collected at the CERN SPS in 2015. This paper addresses the measurement of several properties of ion events, for example, the energy response in the calorimeter and the ionizing energy loss in BGO crystals. Two simulations based on the physics lists QGSP_ BERT_ FTFP and FTFP_ BERT are performed to validate the energy response in the BGO calorimeter; these agree with the experimental data at approximately the 1% to 6% level for different kinds of ions. We also investigate the quenching effect of BGO crystal and found that, for Z $\geq$
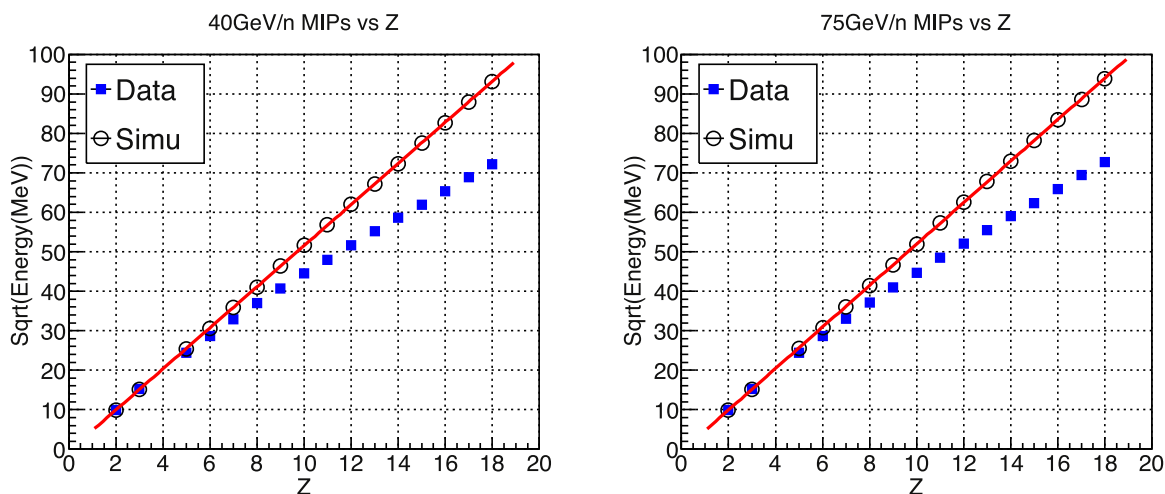
Fig. 13. Square roots of ionization peak energies as a function of the ion atomic number. The blue squares represent the beam data, and the open circles are the MC results.
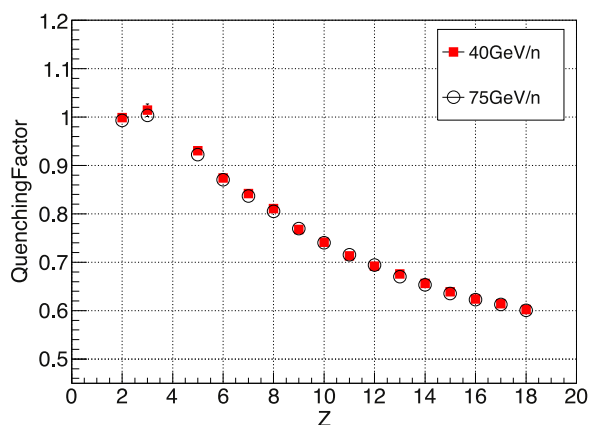

Fig. 14. Measured quenching factors as a function of the ion atomic number for 40 GeV/n (red squares) and 75 GeV/n (open circles). The error bars are statistical errors.

5 particles, the quenching factors are consistent for 40 and 75 GeV/n. The "anti-quenching" effect observed in the CsI(Tl) calorimeter in Fermi LAT beam test is not found in BGO crystal of DAMPE at tens of GeV/n.

Acknowledgments

References

[1] J. Chang, et al., Nature 456 (7220) (2008) 362.
[2] L. Accardo, et al., Phys. Rev. Lett. 113 (12) (2014) 121101.
[3] M. Aguilar, et al., Phys. Rev. Lett. 113 (12) (2014) 121102.
[4] M. Ackermann, et al., Phys. Rev. D 91 (12) (2015) 122002.
[5] J.P. Wefel, et al., Proceedings (ICRC) (2007) 31–34.
[6] Y. Yoon, et al., Astrophys. J. 839 (1) (2017) 5.
[7] O. Adriani, et al., Science 332 (6025) (2011) 69–72.
[8] M. Aguilar, et al., Phys. Rev. Lett. 114 (17) (2015) 171103.
[9] M. Aguilar, et al., Phys. Rev. Lett. 115 (21) (2015) 211101.
[10] J. Chang, et al., Astropart. Phys. 95 (2017) 6–24.
[11] VA160 datasheet and VATA160 datasheet, Integrated Detector Electronics AS (IDE AS), Available: http://www.ideas.no.
[12] AD976A datasheet, Analog Devices. Available: http://www.analog.com/en/products/ad976a.html.
[13] Z. Zhang, et al., Nucl. Instrum. Methods Phys. Res. A 780 (2015) 21–26.
[14] Y. Zhang, et al., Chin. Phys. C 36 (1) (2012) 71.
[15] Y. Wei, et al., IEEE Trans. Nucl. Sci. 63 (2) (2016) 548–551.
[16] C. Feng, et al., IEEE Trans. Nucl. Sci. 62 (6) (2015) 3117–3125.
[17] Z. Zhang, et al., Nucl. Instrum. Methods Phys. Res. A 836 (2016) 98–104.
[18] C. Wang, et al., Chin. Phys. C 41 (10) (2017) 106201.
[19] J. Tammen, et al., Nucl. Instrum. Methods Phys. Res. B 360 (2015) 129–138.
[20] B. Lott, et al., Nucl. Instrum. Methods Phys. Res. A 560 (2) (2006) 395–404.